

Suppression of Dynamically Induced Stochastic Magnetic Behavior Through Materials Engineering

T.J. Broomhall,¹ A.W. Rushforth², M.C. Rosamond,³ E.H. Linfield,³ and T.J. Hayward^{1,*}

¹*Department of Materials Science and Engineering, University of Sheffield, Sheffield, United Kingdom*

²*School of Physics and Astronomy, University of Nottingham, Nottingham NG7 2RD, United Kingdom*

³*School of Electronic and Electrical Engineering, University of Leeds, Leeds, United Kingdom*



(Received 8 October 2019; revised manuscript received 11 December 2019; accepted 15 January 2020; published 14 February 2020)

Stochastic behavior fundamentally limits the performance and reliability of nanomagnetic devices. Typically, stochastic behavior is assumed to be the result of simple thermal activation, but it may also be “dynamically induced,” i.e., a direct result of the spatial and temporal complexity of magnetization dynamics. Here, we show how materials engineering can be used to comprehensively suppress dynamically induced stochasticity. Using the dynamics of magnetic domain walls in $\text{Ni}_{80}\text{Fe}_{20}$ nanowires as a case study, we show how manipulation of the Gilbert damping constant via doping with the rare-earth-element terbium dramatically simplifies domain-wall dynamics. This allows us to obtain quasi-deterministic behaviors from systems that nominally exhibit exceptionally high levels of stochasticity.

DOI: [10.1103/PhysRevApplied.13.024039](https://doi.org/10.1103/PhysRevApplied.13.024039)

I. INTRODUCTION

Overcoming stochastic behavior is one of the great challenges of developing information storage and processing technologies based on nanopatterned magnetic materials. For example, the areal density (numbers of bits stored per inch^2) in conventional magnetic hard disk drives is fundamentally limited by the “trilemma” of magnetic data storage [1], the key consideration of which is preventing the random reversal of data bits. Similar considerations must also be made in the design of solid-state magnetic random access memory (MRAM) cells, where stochastic effects can cause both data loss and result in write errors when the states of the devices are intentionally addressed [2].

Stochastic effects in magnetic devices are typically assumed to be caused by thermal activation, as described by Néel-Brown theory [3]. These can be suppressed by careful materials engineering, for example, by strengthening a material’s magnetocrystalline anisotropy to increase the energy barrier between magnetization states. However, stochastic behavior can also arise from the inherent spatial and temporal complexity of magnetization dynamics [4–10]. A notable example of this occurs in the propagation of magnetic domain walls (DWs) in nanowires composed of the soft ferromagnetic material $\text{Ni}_{80}\text{Fe}_{20}$ [11–17]. These were studied extensively in early efforts to create racetrack memory devices [18,19] and remain relevant to

a diverse range of device applications [20–30] and studies of fundamental magnetic behaviors [5,31,32].

When propagated by magnetic fields [33] or electric currents [34] above a critical threshold, DWs undergo a process known as Walker breakdown [35], where their internal magnetization structures undergo complex and continuous cycles of transformation [36,37]. These transformations cause variable interactions with defect sites and result in both stochastic DW pinning, where inhibition of DW propagation by a defect becomes probabilistic [12,14,17,38,39], and stochastic DW depinning, where the distribution of fields and currents required to depin DWs from defects adopt multimode characters [11,13,15,16,38,39]. We refer to these technologically inhibitive phenomena as “dynamically induced” stochastic effects to differentiate them from their simpler thermally activated counterparts. While propagating DWs at fields and currents below the level of Walker breakdown offers a route to suppressing dynamically induced stochasticity [14,15], Walker breakdown fields and currents typically lie below those required to initiate DW propagation (for example, due to pinning by edge roughness), meaning that no regime is available where DWs can be propagated without exhibiting stochastic behaviors.

Here, we demonstrate that materials engineering can be used to comprehensively suppress dynamically induced stochastic effects in DW devices. We show that, by manipulating the nanowires’ Gilbert damping constants via doping with the rare-earth-element terbium, we can push the onset of complex Walker breakdown dynamics outside of the devices’ normal operating windows (i.e., the applied

*t.hayward@sheffield.ac.uk

fields required to inject and propagate DWs). This greatly simplifies the dynamics of the DWs, such that they exhibit consistent and repeatable interactions with defect sites. Thus, by addressing the root cause of the DWs' stochastic behaviors, we obtain simple quasi-deterministic switching behaviors from devices that are nominally highly stochastic. In doing so, we provide a powerful illustration of how materials engineering can be used to produce inherently reliable device behavior, even in systems where the origin of stochasticity lies beyond that of simple thermal activation.

II. METHODS

To examine the effect of the Gilbert damping constant on the stochasticity of DW pinning, we first deposit both undoped and 5% Tb-doped $\text{Ni}_{80}\text{Fe}_{20}$ precursor thin films by cosputtering from $\text{Ni}_{80}\text{Fe}_{20}$ and Tb targets onto naturally oxidized Si substrates. All films have a thickness of 20 nm and are capped by a 2-nm thick layer of Ru to prevent oxidation. The precursor films are then fabricated into 400 nm wide nanowires via ion milling through a thermally evaporated Al/Ti hard mask and patterned by electron beam lithography and lift-off processing.

The thin film's field-angle resolved hysteresis loops are measured using a home-built magento-optic Kerr effect (MOKE) magnetometer (spot size, several 100s of μm) with a maximum field amplitude of $H = \pm 300$ Oe. These allow extraction of film's easy-axis coercivities, H_c , and anisotropy fields, H_K . The films' Gilbert damping constants, α , and saturation magnetizations, M_s , are measured by field-swept ferromagnetic resonance (FMR) measurements using a vector network analyzer (VNA) FMR system operating in a one-port (reflection) mode. Measurements typically produce mixing of the real and imaginary parts of the dynamic susceptibility, which we correct for in our fitting using the approach of Kalarickal *et al.* [40]. Values of M_s are extracted by fits to the Kittel equation [40]:

$$f_{\text{res}} = \frac{\mu_0 \gamma}{2\pi} \sqrt{(H + H_K)(H + H_K + M_s)}, \quad (1)$$

where f_{res} is the film's FMR frequency at applied field H , H_K is the film's anisotropy field, γ is the gyromagnetic ratio, and μ_0 is the permeability of free space. Values of α are extracted from the variation of the field-swept FMR line width, ΔH , with excitation frequency, f , using [40]

$$\Delta H = \Delta H_0 + \frac{4\pi\alpha f}{|\gamma|\mu_0}, \quad (2)$$

where ΔH_0 is the film's extrinsic FMR line width.

Measurements of the magnetization switching of the nanowires are performed using a home-built focused MOKE (FMOKE) with a laser spot size of about

3 μm . Signal-to-noise levels are high enough to allow measurement of individual switching events with a high-degree of fidelity.

Figure 1(a) illustrates the geometry of the nanowire devices we characterize in this study. The devices consist of 400-nm wide and 20-nm thick $\text{Ni}_{80}\text{Fe}_{20}$ nanowires connected to $10 \times 10 \mu\text{m}^2$ nucleation pads, which are used to inject DWs into the nanowires. Nanowires of this geometry are expected to favor vortex DW (VDW) configurations with either clockwise (CW) or anticlockwise (ACW) chirality [41–43]. Lithographically patterned notches, placed at the midpoint of the nanowires, are used as artificial defect sites at which to probe the stochasticity of DW pinning. The defect sites are patterned in symmetrical “double-notch” configurations to ensure that our results are not distorted by VDWs exhibiting chirality-dependent interactions with the defect sites, as would occur for asymmetric single-notch designs [11]. To characterize the pinning of the DWs at the notches, we perform FMOKE measurements at locations both before and after the defect sites in each nanowire under study [Fig. 1(a)]. A sinusoidal applied field with amplitude ± 300 Oe is continuously cycled at a rate of 27 Hz, while 100 single-shot hysteresis loops are obtained at each location. These allow us to reconstruct the DW's IFDs (applied fields required to

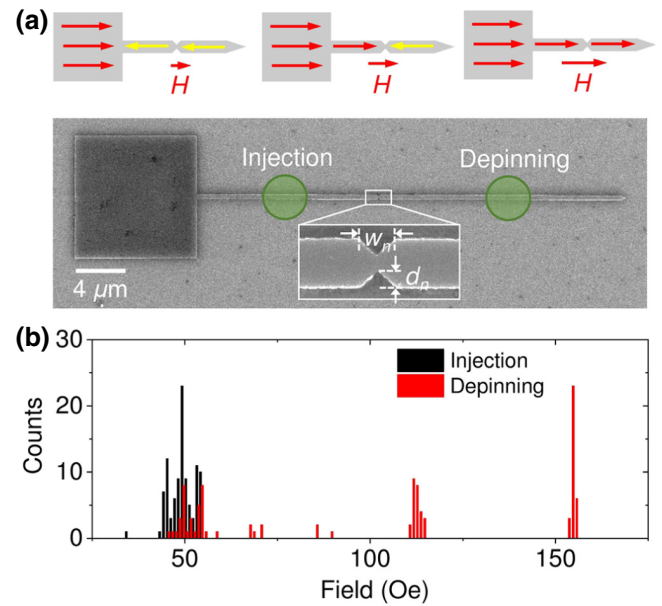


FIG. 1. (a) SEM images illustrating the geometry of the nanowire devices studied. Green circles illustrate the approximate position of the FMOKE laser spot when characterizing a device's injection field distributions (IFDs) and depinning field distributions (DFDs). The schematic at the top of the figure illustrates how the magnetization configuration of the devices is expected to evolve as the applied field is increased. (b) Examples of IFDs and DFDs measured from a $\text{Ni}_{80}\text{Fe}_{20}$ nanowire device with $d_n = 85$ nm and $w_n = 215$ nm.

move the DW from the pad to the defect site) and DFDs (fields required to move the DW from the notch to the end of the nanowire).

Our understanding of the experimental measurements is supported by micromagnetic simulations of DW dynamics, performed using the graphics processing unit-accelerated Mumax [3] simulation package [44]. Simulations use meshes of either $2.5 \times 2.5 \times 2.5 \text{ nm}^3$ or $2 \times 2 \times 2 \text{ nm}^3$, depending on which is required to achieve convergence. Moving simulation windows are used to keep the DW centered in the mesh during propagation in all simulations, except those where the DW's interactions with defect sites are explicitly modeled. Values of M_s and α are taken from the results of FMR measurements, while the exchange stiffness is given a standard value of $A_{\text{ex}} = 13 \text{ pJ m}^{-1}$. The film's weak magnetocrystalline anisotropies are neglected due to the dominance of shape anisotropy on the DW's behavior.

III. RESULTS AND DISCUSSION

We begin with an illustration of how stochastic DW pinning typically manifests in $\text{Ni}_{80}\text{Fe}_{20}$ nanowire devices. Figure 1(b) presents typical IFDs and DFDs measured for a $\text{Ni}_{80}\text{Fe}_{20}$ nanowire containing notches with a depth of $d_n = 85 \text{ nm}$ and width of $w_n = 215 \text{ nm}$. While the IFD is relatively well defined, consisting of a few tightly spaced peaks at about 50 Oe, the DFD is highly stochastic and exhibits both key dynamically induced stochastic phenomena that are typically observed for such nanowire devices [38]. Stochastic pinning can be observed in the partial overlapping of the IFD and DFD, which indicates that a sizeable fraction of DWs pass through the defect site without stopping. Stochastic depinning can be observed in the multimode character of the DFD, with each mode representing a distinct DW configuration becoming pinned at the defect site [4,7,39].

To engineer magnetic materials that inherently suppress dynamically induced stochastic pinning phenomena, we adopt an approach we previously demonstrated in a micromagnetic modeling-based study [43]. The Walker breakdown field (H_{WB}), which represents the point of onset of dynamically induced stochastic effects, is predicted to increase in proportion to the Gilbert damping constant, α , in simple analytical models [43]. Thus, by enhancing α it is expected to be possible to push H_{WB} beyond a device's normal operating field and current range, stabilizing DW motion, and thus, suppressing stochasticity.

Doping $\text{Ni}_{80}\text{Fe}_{20}$ with rare-earth elements (Tb, Ho, Dy) is shown to increase the Gilbert damping constant from its nominal value of $\alpha = 0.007$, with about 5% doping being sufficient to produce enhancements of around an order of magnitude [45–47]. The enhancement of damping with rare-earth concentration is explained by the slow relaxing rare-earth impurity model [46]. Nanowires fabricated from

the 5% Tb-doped $\text{Ni}_{80}\text{Fe}_{20}$ precursor films are expected to increase H_{WB} from typical values of about 10 Oe to close to 100 Oe, which is well outside the range of typical DW propagation fields ($< 50 \text{ Oe}$).

To establish that the Tb-doped $\text{Ni}_{80}\text{Fe}_{20}$ films retain properties suitable for fabricating nanowire devices, we characterize their magnetic properties using MOKE magnetometry and compare them to those of undoped films [Figs. 2(a) and 2(b)]. In both cases, the films exhibit weak uniaxial anisotropy and soft magnetic properties. The addition of Tb results in a modest enhancement of the easy-axis coercivity from $H_c = (3.30 \pm 0.05) \text{ Oe}$ to $H_c = (10.0 \pm 0.5) \text{ Oe}$, and an increase in the anisotropy field (as estimated from the value of the films' saturation fields measured along their hard axes) from $H_K = (18 \pm 1) \text{ Oe}$ to $H_K = (61 \pm 3) \text{ Oe}$, with both these changes likely to be due to Tb doping inducing a small increase in the films' magnetocrystalline anisotropy constants [45]. We also note a slight “double step” in the easy-axis hysteresis loop of the doped film, and we attribute this to competition between the shape anisotropy of the film's (approximately rectangular) substrate and the growth-induced anisotropy of the film, which is misaligned by about 30° from the closest substrate edge. Critically, the coercivities of the Tb-doped films lie below typical injection fields for DW devices (approximately 50 Oe [4,39]), and their anisotropy fields are substantially less than those that would be created by shape anisotropy upon patterning them into nanowires with a $400 \times 20 \text{ nm}^2$ cross section (approximately 580 Oe [48]). We therefore conclude that the Tb-doped films are well suited for patterning into nanowire devices.

Values of α for the Tb-doped and undoped films are measured using VNA FMR. Figure 2(c) presents plots of the frequency dependence of the films' field-swept line widths, from which values of α are extracted by fits to Eq. (1). The Tb-doped film is found to have $\alpha_{\text{Tbdoped}} = 0.120 \pm 0.005$, which is substantially higher than the value of $\alpha_{\text{undoped}} = 0.0059 \pm 0.0001$ measured for the undoped film. This difference in α can be seen to manifest clearly in the differing gradients of the plots in Fig. 2(c), as well as in the widths of individual resonance peaks [see inset to Fig. 2(c)].

Fits of the field dependence of the film's FMR resonance field frequency using Eq. (2) allow the extraction of their saturation magnetizations, with the Tb-doped film exhibiting a value of $M_s = (635 \pm 5) \text{ kA/m}$, which is lower than the value of $M_s = (938 \pm 1) \text{ kA/m}$ obtained for the undoped film. The reduction in M_s for Tb-doped films is well known and occurs due to the antiferromagnetic coupling of Tb moments to the ferromagnetically coupled Ni and Fe moments [45,46]. We note that the values of α and M_s for the undoped films are lower and higher, respectively, than would be expected for stoichiometric

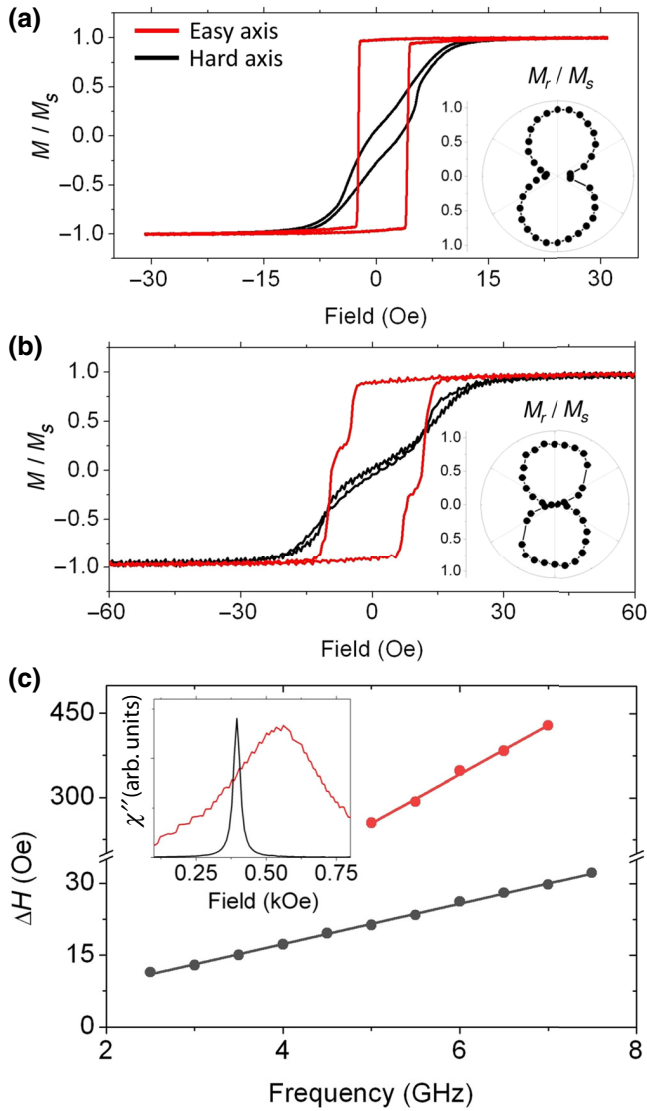


FIG. 2. (a) Easy- and hard-axis hysteresis loops obtained from a 20-nm thick $\text{Ni}_{80}\text{Fe}_{20}$ thin film. Inset presents a polar plot of the film's remanence values. (b) Equivalent hysteresis loops and polar plots for a 20-nm thick $\text{Ni}_{80}\text{Fe}_{20}$ thin film doped with 5% Tb. (c) Variation of the field-swept FMR line width with frequency for undoped (black circles) and 5% Tb-doped (red circles) $\text{Ni}_{80}\text{Fe}_{20}$ thin films. Inset presents illustrative plots of the imaginary parts of the film's susceptibilities (χ''). Black curve, $\text{Ni}_{80}\text{Fe}_{20}$ film, 6 GHz excitation; red curve, 5% Tb-doped $\text{Ni}_{80}\text{Fe}_{20}$, 6.5 GHz excitation.

$\text{Ni}_{80}\text{Fe}_{20}$ films, perhaps suggesting that they are slightly iron rich.

To estimate the degree to which the enhanced damping of the Tb-doped films would suppress Walker breakdown dynamics, we perform micromagnetic simulations of DW propagation in nanowires matching the experimental geometry. Figure 3(a) presents the variation of simulated DW velocity with applied field for nanowires with material properties matching those of both the Tb-doped

and undoped films. The data for the undoped nanowire follow the established form for DWs in soft ferromagnetic nanowires [33,38]: Initially, the velocity of the DW increases linearly with applied field, with this trend terminating at $H_{\text{WB}} = 4$ Oe. After this point, DW motion enters the oscillatory regime, where the DW structure undergoes periodic cycles of transformation, resulting in a dramatic reduction in velocity. The velocity of the DW then remains constant until approximately $H = 40$ Oe, at which point it starts to increase again due to the DW entering the turbulent regime of motion, where the periodicity of the DW transformations breaks down. In contrast to this, the plot for the Tb-doped nanowires shows a simple monotonic trend, indicating that H_{WB} increases to a point beyond the plotted field range. Our simulations suggest that $H_{\text{WB}} > 100$ Oe for the doped nanowires.

Figures 3(b)–3(d) present DW dynamics for two particular simulations: propagation at $H = 50$ Oe in the undoped nanowire and at $H = 35$ Oe in the Tb-doped nanowire. We select these two fields because, as we show below, they represent the mean DW injection fields for nanowires fabricated from the precursor films. Figure 3(b) illustrates the time dependence of the DW positions under these conditions. The data for the undoped nanowire show quasi-periodic oscillations, suggesting that the mean injection field for these devices lies just above the boundary between the oscillatory and turbulent regimes of motion. This is consistent with the DW dynamics shown in Fig. 3(c), where the DW is continuously transforming between VDW-like and transverse DW-like (TDW-like) configurations. In contrast to this, the position of the DW in the Tb-doped nanowire increases monotonically with time [Fig. 3(d)], and the DW retains a consistent VDW magnetization structure, confirming that the mean injection field in these devices lies in the viscous regime of DW motion, below H_{WB} . While exact quantitative agreement between our micromagnetic simulations and the DW dynamics in the devices is not expected, the large differences between the injection fields and Walker breakdown fields in both sets of simulations allow us to have confidence that DWs would propagate with stable magnetization structures in the doped nanowires and unstable structures in the undoped nanowires. Nanowires fabricated from the Tb-doped films are thus expected to show substantially more deterministic behavior than that of equivalents fabricated from the undoped films. We also note that, despite DW mobility in the viscous regime typically decreasing with increasing α , DWs in the doped nanowires are predicted to propagate slightly faster than those in the undoped nanowires at their typical injection fields, due to the suppression of Walker breakdown in the doped devices.

Having demonstrated that H_{WB} should be substantially increased in nanowires with the material properties of the Tb-doped film, we fabricate nanowire devices similar to

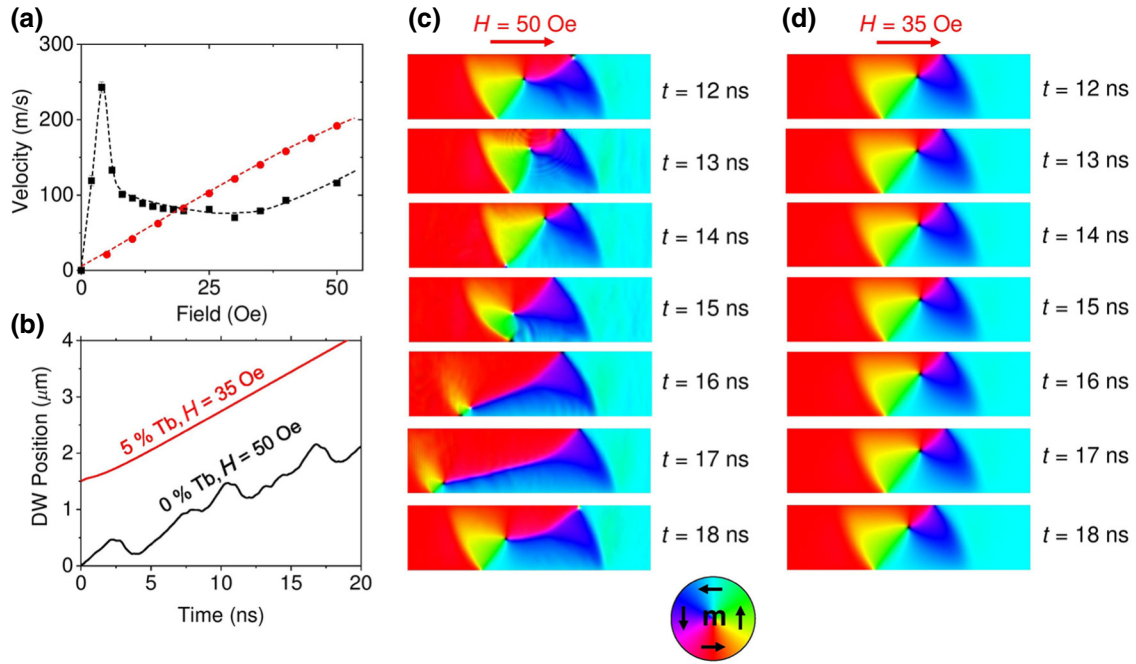


FIG. 3. (a) Micromagnetically calculated domain wall velocities versus applied field in $\text{Ni}_{80}\text{Fe}_{20}$ (black squares) and 5% Tb-doped $\text{Ni}_{80}\text{Fe}_{20}$ nanowires (red circles). (b) Simulated plots of domain wall position versus time at the average injection fields of the undoped and 5% Tb-doped nanowires. Plots are distributed vertically to improve visibility. (c) Simulated domain wall dynamics at $H = 50$ Oe in an undoped nanowire. The mesh window is dynamically centered on the domain wall in each iteration of the simulation. (d) Simulated DW dynamics at $H = 35$ Oe in a Tb-doped nanowire.

those shown in Fig. 1(a) from both the Tb-doped and undoped films and characterize their IFDs and DFDs using FMOKE measurements. For the Tb-doped nanowires (the primary focus of the study), eight devices are measured per defect geometry, with the final data set restricted to devices that exhibit (a) typical injection fields ($H_{\text{inject}} < 50$ Oe) and (b) an absence of additional domain wall pinning sites between the pad and the lithographically patterned notch defect. Additional pinning sites are easily identified as steps in the nanowires' hysteresis loops at FMOKE laser spot positions between the nucleation pad and the notch. We restrict our final data set in this way to ensure that our understanding of the dynamic interactions of the DWs with the notch defects is not distorted by (a) DWs in some devices interacting with the notches at anomalously high fields or (b) by additional defect sites introducing chirality-filtering effects (and thus, additional stochasticity) prior to the DW's interactions with the notches. Applying these criteria restricts our data set to between four and six devices per notch geometry. For the undoped nanowires, which act as a reference data set, four nanowires are measured per defect geometry. All of these devices are found to meet the criteria above and contribute to our final dataset. We suspect that the difference in the viability of devices between the doped and undoped nanowires is due to the enhanced reliability of pinning in the Tb-doped devices (see below), which means that even

small edge defects could pin DWs. Similar defects are likely to be passed through dynamically in the undoped nanowires [17].

Figures 4(a)–4(d) present representative examples of measurements for nanowires containing defects with a variety of sizes ($d_n = 40$ –165 nm and $w_n = 130$ –375 nm). A more comprehensive set of results, comprising measurements from a minimum of four devices for each defect geometry and material combination can be found in the Supplemental Material [49].

Data from the undoped nanowires, for all defect sizes, exhibit highly stochastic DW pinning and depinning. Each nanowire exhibits multimode DFDs, which indicates that DWs with different magnetization structures are pinning at the defect sites, while nanowires with smaller notches exhibit substantial overlap between their IFDs and DFDs, which indicates that pinning is probabilistic. Thus, the data show all key features of dynamically induced stochastic DW behavior, as one would expect when DWs are incident upon a defect site at fields above H_{WB} .

In striking contrast to this, the devices fabricated from the Tb-doped films show quasi-deterministic behavior. Most notably, for all defect sizes, DFDs and IFDs are well separated, which indicates that DWs pin 100% reliably at the defect (i.e., complete suppression of stochastic pinning effects). Furthermore, the majority of devices (11/20) exhibit sharp single-mode DFDs, which indicates that

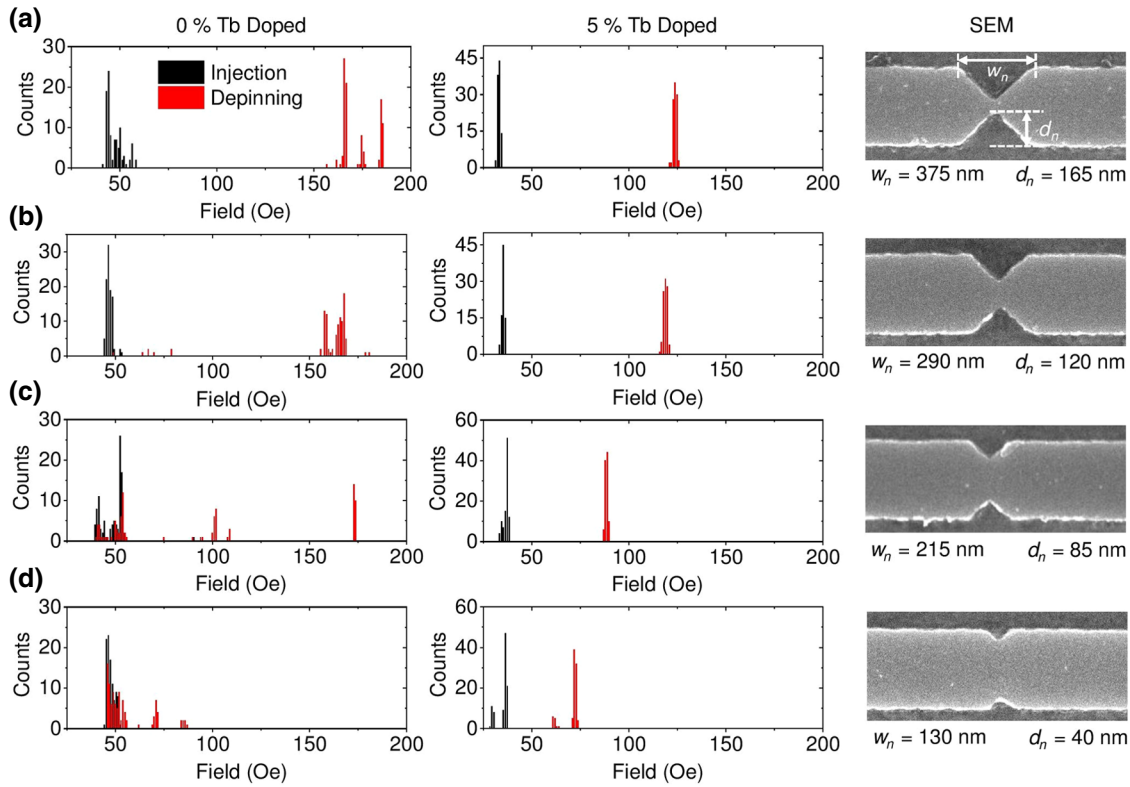


FIG. 4. IFDs and DFDs measured from undoped $\text{Ni}_{80}\text{Fe}_{20}$ and 5% Tb-doped nanowires for a variety of artificial defect sizes. SEM images at the right-hand side of the figure show representative defect shapes and dimensions for each geometry studied.

DWs pin with a consistent magnetization structure. The remaining devices exhibit more than one mode [see, for example, Fig. 4(d)], but these remain relatively tightly distributed (typically within approximately 30 Oe), such that, for a given defect geometry, the DFD is notably narrower in the Tb-doped nanowires (i.e., significant suppression of stochastic depinning). We will return to the question of why these devices show residual stochasticity in their DFDs, despite DWs propagating to the defect sites at fields significantly below H_{WB} , shortly.

The contrasting behavior of the two sets of devices is illustrated further in Figs. 5(a)–5(c), which present mean values of the DFDs (\bar{H}_d), pinning probabilities, and DFD standard deviations ($\bar{\sigma}_{\text{depin}}$) as a function of d_n . In all three plots, each data point represents an average of the parameter in question taken across the measured devices with identical notch depths, d_n , and material compositions. Error bars in Figs. 5(a)–5(c) represent the standard deviation of the data set contributing to that point, rather than the standard error, to give the reader a clear indication of the spread of values across the devices measured.

Figure 5(a) shows that, for both the Tb-doped and undoped nanowires, \bar{H}_d increases monotonically with d_n , as would be expected from the increased pinning potentials that larger defects present. We note that the variation is substantially greater for the undoped nanowires, and we

attribute this feature to the fractional pinning probabilities of these nanowires, which bias the means of the DFDs towards lower values for lower values of d_n .

The dependence of the pinning probabilities on d_n are presented in Fig. 5(b), where it can be seen that the undoped nanowires show highly stochastic pinning for $d_n < 100$ nm, replicating trends seen in several of our previous studies [4,39]. In contrast to this, the Tb-doped nanowires exhibit 100% reliable pinning for each of the defect geometries studied.

A more generalized expression of the stochasticity is provided by $\bar{\sigma}_{\text{depin}}$ [Fig. 5(c)], which we consider here as a crude measure of DFD spread. For the Tb-doped nanowires, $\bar{\sigma}_{\text{depin}}$ is typically just a few oersted, emphasizing the highly repeatable switching in these devices. The values of $\bar{\sigma}_{\text{depin}}$ for the undoped nanowires are universally higher than this, peaking at $\bar{\sigma}_{\text{depin}} = 34$ Oe for $d_n = 85$ nm, which is an enhancement of about 1400% over the value of $\bar{\sigma}_{\text{depin}} = 2.4$ Oe observed for equivalent Tb-doped nanowires. We note that the relatively low value of $\bar{\sigma}_{\text{depin}} = 9.5$ Oe observed for the smallest defects ($d_n = 40$ nm) in the undoped nanowires is purely a consequence of the low pinning probability (i.e., the DFD overlaps strongly with the relatively narrow IFD), and thus, is somewhat misleading. On the other hand, the low value of $\sigma_{\text{depin}} = 7.7$ Oe for the largest defect sites ($d_n = 165$ nm)

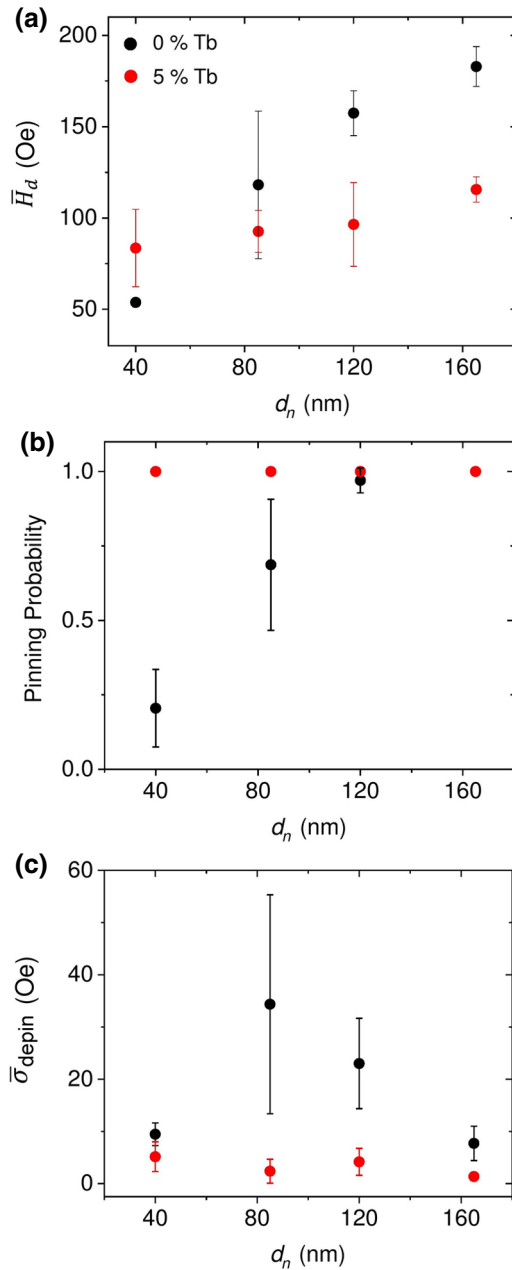


FIG. 5. (a) Mean depinning field (\bar{H}_d) as a function of notch depth (d_n) for undoped $\text{Ni}_{80}\text{Fe}_{20}$ (black circles) and 5% Tb-doped (red circles) nanowires. (b) Mean pinning probability as a function of notch depth. (c) Mean DFD standard deviation ($\bar{\sigma}_{\text{depin}}$) as a function of notch depth. In all three plots, each data point represents an average of the parameter in question taken across measured devices with nominally identical notch depths, d_n , and material compositions. Error bars in all three figures represent the standard deviation of the data set contributing to the point, rather than the standard error, to give the reader a clear indication of the spread of values across the devices measured.

in the undoped nanowires genuinely reflects the tendency for dynamically induced stochastic effects to be less significant for larger defect sites [4,39], and yet is still about

600% larger than the value for equivalently sized defects in the doped nanowires. These trends are maintained even when we normalize σ_{depin} to H_{depin} to take account of generally higher depinning fields in the undoped nanowires (see the Supplemental Material [49]).

We note here that, while previous work has shown that, even in undoped nanowires, rare defect geometries can be found that minimize stochasticity [4,39], we observe substantial improvements in both metrics of stochasticity (pinning probability and $\bar{\sigma}_{\text{depin}}$) across all defect geometries in the doped nanowires. This suggests that these improvements originate in the material properties of the nanowires, rather than being an accident of device geometry.

While the results presented above clearly demonstrate that stochastic behavior is dramatically suppressed in the Tb-doped nanowires, we now return to the origin of the small degree of DFD splitting observed in a minority of these devices. This is unexpected because suppression of Walker breakdown should result in the DWs adopting singular well-defined magnetization configurations, when pinned at defect sites, and thus, single-mode DFDs. In several nanowires [e.g., Fig. 4(d)], splitting in both the IFD and DFD appear simultaneously, prompting us to investigate whether there is a causal relationship between bimodal and split IFDs and split DFDs, and a Pearson's χ^2 test ($\chi^2 = 5.09$ and $P = 0.024$) rejects the null hypothesis that these features are uncorrelated across the data set at $P < 0.05$ (see the Supplemental Material [49]).

To explain the correlation between splitting in the IFDs and DFDs, we further study the nanowires' behaviors using micromagnetic simulations. We first note that these results indicate that the total energy of TDWs is only 30% greater than that of VDWs in the doped nanowires and that both types of DWs can propagate stably at typical injection fields. Thus, the doped nanowires could feasibly support six distinct propagating DW structures: TDWs with up or down chiralities and VDWs with ACW or CW chiralities and up or down vortex core polarizations. We suggest that, in devices where the IFDs are split (i.e., exhibit multiple reversal modes), multiple forms of DWs are being injected into the nanowires. The different ways in which these pin at a given defect site would then result in subsequent splitting of the DFD. We note that, even in devices with single-mode IFDs, it is possible that different DW structures can be injected, for example, through the effects of thermal perturbations at critical points in the injection process. Furthermore, different injection modes might not always result in different DW structures being injected. Potentially, this explains why splitting of the IFDs and DFDs is not perfectly correlated across our data set.

To test this hypothesis, we use micromagnetic simulations to examine the pinning and depinning of each possible DW structure at a defect site, replicating the geometry of the double notches shown in Fig. 4(d) ($d_n = 40$ nm). Details of these simulations are presented in Fig. S6 within

the Supplemental Material [49]. The simulations show that DWs can exhibit three distinct depinning fields: $H = 60$ (ACW VDW with core up or down), 75 (CW VDW with core down), and 85 Oe (TDW up, TDW down, CW VDW with core up). The range of these depinning fields corresponds closely to that observed for experimental devices with similar notch geometries (Fig. S4 within the Supplemental Material [49]). Thus, we conclude the small degree of DFD stochasticity observed in a minority of the Tb-doped devices is likely to be due to variability in the magnetization structure of injected DWs, as opposed to inherently stochastic interaction of the DWs with the defect sites. This is an important distinction because many studies have demonstrated the feasibility of controlling the initial structure and chirality of DWs [6,24,50,51], while the dynamic interactions of DWs with defect sites is inherently uncontrollable at fields above H_{WB} [38]. Clearly, methods of controlling the structure of nucleated DWs will need to be employed in future devices to obtain fully reliable operations.

DWs in soft magnetic nanowires are known to strongly manifest dynamically induced stochasticity, and thus, they are expected to benefit dramatically from the materials engineering approach we demonstrate here. However, it is interesting to ask whether the approach might have broader utility. To examine this, we consider the $10 \times 10 \mu\text{m}^2$ nucleation pads attached to the nanowires' ends. These represent more generic examples of mesoscopic magnetic systems and are expected to exhibit complex two-dimensional magnetization states [52], the details of which would dictate the manner in which DWs are injected into the nanowires. Thus, the widths of IFDs are expected to offer a probe of how stochastic the switching behavior of these large complex magnetic microstructures is.

A cursory examination of the IFDs shown in Fig. 4 appear to indicate that the IFDs for the undoped nanowires are typically wider and more complex than those for the Tb-doped nanowires. Quantitatively, we find that the mean of the IFD standard deviations is $\sigma_{\text{inject}} = (3.8 \pm 0.6)$ Oe for the undoped nanowires, compared with $\sigma_{\text{inject}} = (1.6 \pm 0.3)$ Oe for the Tb-doped nanowires. This striking reduction in stochasticity remains significant, even when these results are normalized by the nanowires' mean injection fields (undoped nanowires, $\sigma_{\text{inject}}/H_{\text{inject}} = 0.078 \pm 0.012$; Tb-doped nanowires, $\sigma_{\text{inject}}/H_{\text{inject}} = 0.045 \pm 0.010$). These additional results thus provide evidence that engineering the dynamic behavior of magnetic materials to reduce stochasticity can find utility in a wider range of systems than those we primarily study here.

IV. CONCLUSIONS

We demonstrate that materials engineering can be used to control dynamically induced stochastic behavior in

magnetic nanostructures. Using the pinning of DWs in $\text{Ni}_{80}\text{Fe}_{20}$ nanowires as a case study, we show how enhancing the damping constant of magnetic materials via doping with rare-earth elements allows us to obtain simple quasi-deterministic switching behavior from systems that nominally show exceptionally complex stochastic behaviors. Our work demonstrates that engineering basic magnetic properties offers a viable route to regulate device behavior, even when stochasticity is caused by the inherent spatial and temporal complexity of magnetization dynamics, rather than by simple thermal activation processes.

More directly, our results have potential implications for devices based on the propagation and pinning of DWs in soft ferromagnetic nanowires. For example, we have recently proposed DW logic networks in which binary information is stored and processed within the chirality of VDWs [21,24], and the viability of such architectures will be entirely dependent on stabilizing the DW structure and obtaining reliable DW pinning and depinning. Furthermore, automotive turn sensors based on soft magnetic nanowires are currently the only commercial realization of DW devices [28,29], and their noise performance may be improved by the suppression of stochastic pinning effects. Architecturally similar devices for transporting magnetic micro- and nanoparticles [22,30] and ultracold atoms [25,53,54] may also benefit from smoother more deterministic DW motion. In reality, optimized doping levels would need to be selected. These would be chosen to keep DWs moving at fields just below the Walker breakdown for typical operating fields and currents (thus minimizing stochasticity), while also maximizing the DW mobility, and thus, the operating speeds of devices.

Our work will also have interesting implications for artificial spin ice systems, the dynamics of which are intimately linked to the types of DW dynamics studied here [5,6]. These have proposed applications in the rapidly emerging field of neuromorphic computing [55,56], and the ability to tune the level of stochasticity in such systems may be highly valuable to realizing viable devices.

ACKNOWLEDGMENTS

T.J.H. acknowledges support by the Engineering and Physical Sciences Research Council (Grant No. EP/J002275/1).

- [1] G. W. Qin, Y. P. Ren, N. Xiao, B. Yang, L. Zuo, and K. Oikawa, Development of high density magnetic recording media for hard disk drives: Materials science issues and challenges, *Int. Mater. Rev.* **54**, 157 (2009).
- [2] A. D. Kent and D. C. Worledge, A new spin on magnetic memories, *Nat. Nanotechnol.* **10**, 187 (2015).
- [3] W. F. Brown, Thermal fluctuations of a single-domain particle, *Phys. Rev.* **130**, 1677 (1963).

- [4] T. J. Hayward and K. A. Omari, Beyond the quasi-particle: Stochastic domain wall dynamics in soft ferromagnetic nanowires, *J. Phys. D: Appl. Phys.* **50**, 084006 (2017).
- [5] K. Zeissler, S. K. Walton, S. Ladak, D. E. Read, T. Tylliszczak, L. F. Cohen, and W. R. Branford, The non-random walk of chiral magnetic charge carriers in artificial spin ice, *Sci. Rep.* **3**, 1252 (2013).
- [6] A. Pushp, T. Phung, C. Rettner, B. P. Hughes, S.-H. Yang, L. Thomas, and S. S. P. Parkin, Domain wall trajectory determined by its fractional topological edge defects, *Nat. Phys.* **9**, 505 (2013).
- [7] M. Y. Im, K.-S. Lee, A. Vogel, J.-I. Hong, G. Meier, and P. Fischer, Stochastic formation of magnetic vortex structures in asymmetric disks triggered by chaotic dynamics, *Nat. Commun.* **5**, 5620 (2014).
- [8] A. M. Shutyi and D. I. Sementsov, Magnetization stochastic dynamics in exchange-coupled layered structure title, *JETP Lett.* **78**, 480 (2003).
- [9] D. I. Sementsov and A. M. Shutyi, Nonlinear regular and stochastic dynamics of magnetization in thin-film structures, *Phys.-Usp* **50**, 793 (2007).
- [10] E. Reibold, W. Just, J. Becker, and H. Benner, Stochastic Resonance in Chaotic Spin-Wave Dynamics, *Phys. Rev. Lett.* **78**, 1997 (1997).
- [11] M. Hayashi, L. Thomas, C. Rettner, R. Moriya, X. Jiang, and S. S. P. Parkin, Dependence of Current and Field Driven Depinning of Domain Walls on Their Structure and Chirality in Permalloy Nanowires, *Phys. Rev. Lett.* **97**, 207205 (2006).
- [12] H. Tanigawa, T. Koyama, M. Bartkowiak, S. Kasai, K. Kobayashi, T. Ono, and Y. Nakatani, Dynamical Pinning of a Domain Wall in a Magnetic Nanowire Induced by Walker Breakdown, *Phys. Rev. Lett.* **101**, 207203 (2008).
- [13] M. Y. Im, L. Bocklage, P. Fischer, and G. Meier, Direct Observation of Stochastic Domain-Wall Depinning in Magnetic Nanowires, *Phys. Rev. Lett.* **102**, 147204 (2009).
- [14] M. Muñoz and J. L. Prieto, Suppression of the intrinsic stochastic pinning of domain walls in magnetic nanostripes, *Nat. Commun.* **2**, 562 (2011).
- [15] U. H. Pi, Y.-J. Cho, J.-Y. Bae, S.-C. Lee, S. Seo, W. Kim, J.-H. Moon, K.-J. Lee, and H.-W. Lee, Static and dynamic depinning processes of a magnetic domain wall from a pinning potential, *Phys. Rev. B - Condens. Matter Mater. Phys.* **84**, 024426 (2011).
- [16] J. Briones, F. Montaigne, M. Hehn, D. Lacour, J. R. Childress, and M. J. Carey, Stochastic and complex depinning dynamics of magnetic domain walls, *Phys. Rev. B - Condens. Matter Mater. Phys.* **83**, 060401(R) (2011).
- [17] E. R. Lewis, D. Petit, L. O'Brien, A.-V. Jausovec, H. T. Zeng, D. E. Read, and R. P. Cowburn, Kinetic depinning of a magnetic domain wall above the Walker field, *Appl. Phys. Lett.* **98**, 042502 (2011).
- [18] S. S. P. Parkin, M. Hayashi, and L. Thomas, Magnetic domain-wall racetrack memory, *Science* **320**, 190 (2008).
- [19] S. Parkin and S.-H. Yang, Memory on the racetrack, *Nat. Nanotechnol.* **10**, 195 (2015).
- [20] D. A. Allwood, G. Xiong, C. C. Faulkner, D. Atkinson, D. Petit, and R. P. Cowburn, Magnetic domain-wall logic, *Science* **309**, 1688 (2005).
- [21] K. A. Omari and T. J. Hayward, Chirality-Based Vortex Domain-Wall Logic Gates, *Phys. Rev. Appl.* **2**, 044001 (2014).
- [22] E. Rapoport, D. Montana, and G. S. D. Beach, Integrated capture, transport, and magneto-mechanical resonant sensing of superparamagnetic microbeads using magnetic domain walls, *Lab Chip* **12**, 4433 (2012).
- [23] J. Vandermeulen, B. Van De Wiele, L. Dupré, and B. Van Waeyenberge, Logic and memory concepts for all-magnetic computing based on transverse domain walls, *J. Phys. D: Appl. Phys.* **48**, 275003 (2015).
- [24] K. A. Omari, T. J. Broomhall, R. W. S. Dawidek, D. A. Allwood, R. C. Bradley, J. M. Wood, P. W. Fry, M. C. Rosamond, E. H. Linfield, M.-Y. Im, P. J. Fischer, and T. J. Hayward, Toward chirality-encoded domain wall logic, *Adv. Funct. Mater.* **29**, 1807282 (2019).
- [25] D. A. Allwood, T. Schrefl, G. Hrkcac, I. G. Hughes, and C. S. Adams, Mobile atom traps using magnetic nanowires, *Appl. Phys. Lett.* **89**, 014102 (2006).
- [26] T. J. Hayward, A. D. West, K. J. Weatherill, T. Schrefl, I. G. Hughes, and D. A. Allwood, Nanomagnetic engineering of the properties of domain wall atom traps, *J. Appl. Phys.* **110**, 123918 (2011).
- [27] A. D. West, K. J. Weatherill, T. J. Hayward, P. W. Fry, T. Schrefl, M. R. J. Gibbs, C. S. Adams, D. A. Allwood, and I. G. Hughes, Realization of the manipulation of ultracold atoms with a reconfigurable nanomagnetic system of domain walls, *Nano Lett.* **12**, 4065 (2012).
- [28] R. Mattheis, M. Diegel, U. Hübner, and E. Halder, Multiturn counter using the movement and storage of 180° magnetic domain walls, *IEEE Trans. Magn.* **42**, 3297 (2006).
- [29] R. Mattheis, S. Glathe, M. Diegel, and U. Hübner, Concepts and steps for the realization of a new domain wall based giant magnetoresistance nanowire device: From the available 2 4 multiturn counter to a 2 12 turn counter, *J. Appl. Phys.* **111**, 113920 (2012).
- [30] E. Rapoport and G. S. D. Beach, Architecture for directed transport of superparamagnetic microbeads in a magnetic domain wall routing network, *Sci. Rep.* **7**, 10139 (2017).
- [31] S. Ladak, D. E. Read, G. K. Perkins, L. F. Cohen, and W. R. Branford, Direct observation of magnetic monopole defects in an artificial spin-ice system, *Nat. Phys.* **6**, 359 (2010).
- [32] W. R. Branford, S. Ladak, D. E. Read, K. Zeissler, and L. F. Cohen, Emerging chirality in artificial spin ice, *Science* **335**, 1597 (2012).
- [33] G. S. D. Beach, C. Nistor, C. Knutson, M. Tsoi, and J. L. Erskine, Dynamics of field-driven domain-wall propagation in ferromagnetic nanowires, *Nat. Mater.* **4**, 741 (2005).
- [34] N. Vernier, D. A. Allwood, D. Atkinson, M. D. Cooke, and R. P. Cowburn, Domain wall propagation in magnetic nanowires by spin-polarized current injection, *Europhys. Lett.* **65**, 526 (2004).
- [35] N. L. Schryer and L. R. Walker, The motion of 180° domain walls in uniform dc magnetic fields, *J. Appl. Phys.* **45**, 5406 (1974).
- [36] J. Y. Lee, K. S. Lee, S. Choi, K. Y. Guslienko, and S. K. Kim, Dynamic transformations of the internal structure of

- a moving domain wall in magnetic nanostripes, *Phys. Rev. B - Condens. Matter Mater. Phys.* **76**, 184408 (2007).
- [37] S. K. Kim, J. Y. Lee, Y. S. Choi, K. Y. Guslienko, and K. S. Lee, Underlying mechanism of domain-wall motions in soft magnetic thin-film nanostripes beyond the velocity-breakdown regime, *Appl. Phys. Lett.* **93**, 052503 (2008).
- [38] T. J. Hayward, Intrinsic nature of stochastic domain wall pinning phenomena in magnetic nanowire devices, *Sci. Rep.* **5**, 13279 (2015).
- [39] K. A. Omari and T. J. Hayward, A micromagnetic protocol for qualitatively predicting stochastic domain wall pinning, *Sci. Rep.* **7**, 17862 (2017).
- [40] S. S. Kalarickal, P. Krivosik, M. Wu, C. E. Patton, M. L. Schneider, P. Kabos, T. J. Silva, and J. P. Nibarger, Ferromagnetic resonance linewidth in metallic thin films: Comparison of measurement methods, *J. Appl. Phys.* **99**, 093909 (2006).
- [41] R. D. McMichael and M. J. Donahue, Head to head domain wall structures in thin magnetic strips, *IEEE Trans. Magn.* **33**, 4167 (1997).
- [42] M. Laufenberg, D. Backes, W. Bührer, D. Bedau, M. Kläui, U. Rüdiger, C. A. Vaz, J. A. Bland, L. J. Heyderman, F. Nolting, and S. Cherifi, Observation of thermally activated domain wall transformations, *Appl. Phys. Lett.* **88**, 1 (2006).
- [43] T. J. Broomhall and T. J. Hayward, Suppression of stochastic domain wall pinning through control of gilbert damping, *Sci. Rep.* **7**, 17100 (2017).
- [44] A. Vansteenkiste, J. Leliaert, M. Dvornik, M. Helsen, F. Garcia-Sanchez, and B. Van Waeyenberge, The design and verification of MuMax3, *AIP Adv.* **4**, 107133 (2014).
- [45] W. Bailey, P. Kabos, F. Mancoff, and S. Russek, Control of magnetization dynamics in $\text{Ni}_{81}\text{Fe}_{19}$ thin films through the use of rare-earth dopants, *IEEE Trans. Magn.* **37**, 1749 (2001).
- [46] G. Woltersdorf, M. Kiessling, G. Meyer, J. U. Thiele, and C. H. Back, Damping by Slow Relaxing Rare Earth Impurities in $\text{Ni}_{80}\text{Fe}_{20}$, *Phys. Rev. Lett.* **102**, 257602 (2009).
- [47] T. A. Moore, P. Möhrke, L. Heyne, A. Kaldun, M. Kläui, D. Backes, J. Rhensius, L. J. Heyderman, J.-U. Thiele, G. Woltersdorf, A. Fraile Rodríguez, F. Nolting, T. O. Menteş, M. Á. Niño, A. Locatelli, A. Potenza, H. Marchetto, S. Cavill, and S. S. Dhesi, Magnetic-field-induced domain-wall motion in permalloy nanowires with modified Gilbert damping, *Phys. Rev. B - Condens. Matter Mater. Phys.* **82**, 094445 (2010).
- [48] D. G. Porter and M. J. Donahue, Velocity of transverse domain wall motion along thin, narrow strips, *J. Appl. Phys.* **95**, 6729 (2004).
- [49] See the Supplemental Material at <http://link.aps.org/supplemental/10.1103/PhysRevApplied.13.024039> for histogram/numerical data from each of the devices measured, details of statistical testing, and additional simulation results.
- [50] D. Mcgrouther, S. McVitie, J. N. Chapman, and A. Gentils, Controlled domain wall injection into ferromagnetic nanowires from an optimized pad geometry, *Appl. Phys. Lett.* **91**, 022506 (2007).
- [51] K. Omari, R. C. Bradley, T. J. Broomhall, M. P. P. Hodges, M. C. Rosamond, E. H. Linfield, M.-Y. Im, P. Fischer, and T. J. Hayward, Ballistic rectification of vortex domain wall chirality at nanowire corners, *Appl. Phys. Lett.* **107**, 222403 (2015).
- [52] M. T. Bryan, P. W. Fry, T. Schrefl, M. R. J. Gibbs, D. A. Allwood, M.-Y. Im, and P. Fischer, Transverse field-induced nucleation pad switching modes during domain wall injection, *IEEE Trans. Magn.* **46**, 963 (2010).
- [53] M. Negoita, T. J. Hayward, and D. A. Allwood, Controlling domain walls velocities in ferromagnetic ring-shaped nanowires, *Appl. Phys. Lett.* **100**, 072405 (2012).
- [54] M. Negoita, T. J. Hayward, J. A. Miller, and D. A. Allwood, Domain walls in ring-shaped nanowires under rotating applied fields, *J. Appl. Phys.* **114**, 013904 (2013).
- [55] M. Hehn, F. Montaigne, D. Lacour, Y. Perrin, B. Canals, N. Rougemaille, J. Grollier, D. Querlioz, and A. Masseboeuf, in *Spintronics XI* 121 (2018).
- [56] J. H. Jensen, E. Folven, and G. Tufte, in *ALIFE 2018: The 2018 Conference on Artificial Life*. p. 15.